

STONet: A Neural-Operator-Driven Spatio-temporal Network

Haitao Lin,¹ Guojiang Zhao,¹ Lirong Wu,¹ Stan Z. Li¹

Abstract

Graph-based spatio-temporal neural networks are effective to model the spatial dependency among discrete points sampled irregularly from unstructured grids, thanks to the great expressiveness of graph neural networks. However, these models are usually spatially-transductive – only fitting the signals for discrete spatial nodes fed in models but unable to generalize to ‘unseen’ spatial points with zero-shot. In comparison, for forecasting tasks on continuous space such as temperature prediction on the earth’s surface, the *spatially-inductive* property allows the model to generalize to any point in the spatial domain, demonstrating models’ ability to learn the underlying mechanisms or physics laws of the systems, rather than simply fit the signals. Besides, in temporal domains, *irregularly-sampled* time series, e.g. data with missing values, urge models to be temporally-continuous. Motivated by the two issues, we propose a spatio-temporal framework based on neural operators for PDEs, which learn the underlying mechanisms governing the dynamics of spatially-continuous physical quantities. Experiments show our model’s improved performance on forecasting spatially-continuous physic quantities, and its superior generalization to unseen spatial points and ability to handle temporally-irregular data.

1. Introduction

Studying the spatio-temporal patterns of physical quantities is of great scientific interest. Significant progress has been achieved thanks to immense research efforts in deep neural networks for modeling the spatial dependency and temporal dynamics (Shi et al., 2015; Guo et al., 2019b; Zhao et al., 2020; Bai et al., 2020; Li et al., 2021a). Most of them are established for spatially-discrete nodes, such as sensors’ signals of traffic flow located on discretized roads, and graph neural networks (GNNs) are usually employed to handle signals with spatially-irregular distribution and establish dependency between nodes (Seo et al., 2016; Yu et al., 2018; Li et al., 2018; Rozemberczki et al., 2021). In comparison, models established for spatio-temporal forecasting tasks for spatially-continuous physical quantities are

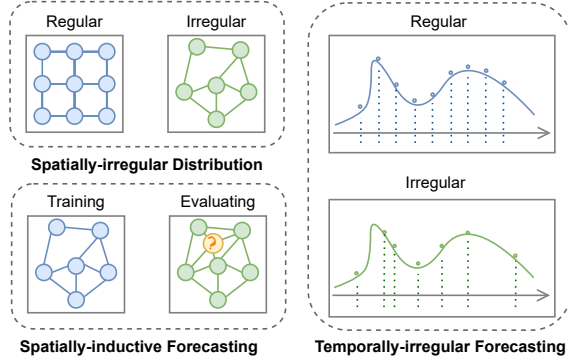


Figure 1. The discussed challenges in spatio-temporal forecasting.

still rare, although in real-world scenarios, the needs for them are urgent. Examples arise in fields like geophysics such as temperature and humidity forecasting (Rasp et al., 2020), where there exists a value of temperature or humidity at every point on the earth’s surface, and acoustic or electromagnetism such as wave equation modeling (Saha et al., 2021). While the previous models for discrete spatial domain can also be used for tasks like weather forecasting (Lin et al., 2021), they are limited to only capturing dynamics of the discrete sample points which are fed in models. However, for points in the continuous spatial domain which have not been seen by the model, they fail to generalize on them well. Besides, in real-world application, time intervals between observations may be non-uniform, such as missing data scenarios, which drives us to construct a model to deal with temporal irregularly-sampled data.

In summary, we conclude three challenges for continuous spatio-temporal models as shown in Fig. 1: (1) modeling the dependency among sample points of *spatially-irregular distribution*, which can be well-solved by GNNs; (2) *spatially-inductive forecasting* and (3) *temporally-irregular forecasting* which are both not been well resolved. To address (2), we aim to introduce a forecasting model that can both predict physical quantities or signals on irregularly-distributed points, and accurately generalize the learned dynamic patterns to the ‘unseen’ points sampled from the continuous spatial domain. Besides, when the time intervals between observations are not equal as (3) discusses, e.g. there are missing timestamps in training data, we want the established model to be continuous in temporal domains and thus can still generate accurate predictions.

Recently, great progress has been achieved in solving partial differential equations (PDEs) (Raissi et al., 2019; Jiang et al., 2020; Greenfeld et al., 2019; Kochkov et al., 2021), which is able to learn the implicit or explicit mechanisms governing the dynamics of spatially-continuous physical quantities. Inspired by this, we deduce that such models can be well generalized to the unseen spatial points and irregularly-sampled timestamps based on the fact that the dynamics governed by PDE models are applicable to any spatial point and time in the domains, and thus build a spatio-temporal model to learn the underlying PDEs for solving issue (2) and (3). On contrary to approaches designed to model one specific instance of PDE (E & Yu, 2017; Bar & Sochen, 2019; Smith et al., 2020; Pan & Duraisamy, 2020; Raissi et al., 2020), our model aims to not be limited to one physical process and approximate different dynamical systems well. Therefore, neural operators (Lu et al., 2021; Bhattacharya et al., 2021; Li et al., 2020a; 2021b; Nelsen & Stuart, 2021) is a desirable option, which directly learn the mapping between infinite-dimensional spaces of functions, requiring no knowledge of underlying PDEs, and only data. We name our model as spatio-temporal operator net (STONET), which first encodes the history observations with graph neural operators, and generates future predictions with universal operators. The multipole-graph-based encoder allows the spatial points to be *irregularly distributed* on unstructured grids, and the neural-operator-driven architecture enables both *spatially-inductive* and *temporally-irregular forecasting*. Our primary contributions include:

- We set up an encoder with historical observations fed in, based on multipole graph operators, which can capture the long-range spatial dependency as well as approximate the mappings of learned parametric functions into solution representation functions. (Sec. 3.1)
- We establish a universal-operator-based decoder, approximating solution representation functions with historical observations, for future predictions. (Sec. 3.2)
- We show our model’s high performance for spatio-temporal forecasting on real-world datasets, points in which are irregularly distributed in continuous spatial domains. Besides, experimental results prove its capability of spatially-inductive and temporally-irregular forecasting with further analysis. (Sec. 5)

2. Background

2.1. Notation and Preliminary

Let F be a multivariate function, and the partial differential equation governing the continuous dynamical system reads

$$\frac{\partial u}{\partial t} = F \left(\mathbf{x}, \frac{\partial u}{\partial x_1}, \dots, \frac{\partial u}{\partial x_m}, \frac{\partial^2 u}{\partial x_1^2}, \frac{\partial^2 u}{\partial x_1 \partial x_2}, \frac{\partial^2 u}{\partial x_2^2}, \dots; \theta \right), \quad (1)$$

where $u = u(\mathbf{x}, t) \in \mathcal{U}$ is the observed physical quantity of m -dimensional spatial location $\mathbf{x} = (x_1, \dots, x_m) \in D$ at time $t \in [0, T]$ with \mathcal{U} a separable Banach space., and $\theta = \theta(\mathbf{x}, t)$ reflects the external influence. For example, in homogeneous heat equation, $\frac{\partial u}{\partial t} = \sum_{i=1}^m \frac{\partial^2 u}{\partial x_i^2} + q$ where u is the temperature, and $\theta = q$ is the heat sources. Note that when the equation describes the dynamics of time, we write $u(\mathbf{x}, t)$ as $u_{\mathbf{x}}(t)$ for fixed spatial location, and as $u_t(\mathbf{x})$ when the equation or operator is with respect to \mathbf{x} . For example, the heat equation can be written as $\frac{\partial u_{\mathbf{x}}}{\partial t} = \sum_{i=1}^m \frac{\partial^2 u_t}{\partial x_i^2} + q$.

2.2. Neural Operator for PDE

Parametric PDEs. Assume that the term on the right side of the Eq. 1 can be parameterized as a parametric PDE, and there exists $f(\mathbf{x}, t)$, such that

$$(\mathcal{L}_{a_t} u_t)(\mathbf{x}) = f(\mathbf{x}, t), \quad (2)$$

where \mathcal{L}_{a_t} is a differential operator with respect to \mathbf{x} , determined by $a_t(\mathbf{x}) \in \mathcal{A}$ with \mathcal{A} a separable Banach space. Because the operator is not with respect to t , t can be regarded as a parameter in u and a , rather than a variable like \mathbf{x} . When the parametric function a_t differs as time varies, $u_t(\mathbf{x})$ also changes over time.

To obtain the solution $u_t(\mathbf{x})$, we aim to approximate a target mapping between two infinite-dimensional function spaces, which is $\mathcal{F} : \mathcal{A} \rightarrow \mathcal{U}$, such that $\mathcal{F}(a_t) = u_t$. Given the $n_t \times n_s$ observations $\{(a_{t_i}(\mathbf{x}_j), u_{t_i}(\mathbf{x}_j)) : i = 1, \dots, n_t, j = 1, \dots, n_s\}$, \mathcal{F}^\dagger is to used to approximate \mathcal{F} such that $\mathcal{F}^\dagger \approx \mathcal{F}$.

Universal operators. When the parametric function $a(\mathbf{x}, t)$ or equation formulation is totally unknown, a universal approximator can be used to directly learn the operator. For a certain $u(\mathbf{x}, t)$, the target operator is \mathcal{G} , given $n_t \times n_s$ observations $\{(u(\mathbf{x}_j, t_i), \mathcal{G}(u)(\mathbf{x}_j, t_i)) : i = 1, \dots, n_t, j = 1, \dots, n_s\}$, we try to establish a universal approximator \mathcal{G}^\dagger , such that $\mathcal{G}^\dagger \approx \mathcal{G}$, according to the provided observations. As such, we can obtain $\mathcal{G}^\dagger(u)(\mathbf{x}, t)$ at any $\mathbf{x} \in D$ and $t \in [0, T]$ as its approximation.

Here are the differences between \mathcal{F} and \mathcal{G} . \mathcal{F} learns a solution mapping shared by PDEs parameterized by a family of operators $\{\mathcal{L}_{a_t}\}_{t \in [0, T]}$ with the same parametric forms \mathcal{L} and different parameters $\{a_t\}$. For example, Eq. 2 governed by the second order elliptic operator $\mathcal{L}_a = -\operatorname{div}(a \nabla \cdot)$ describes many physical phenomenons including hydrology (BearM & Corapcioglu, 2012) and elasticity (Antman, 2005). In comparison, the second one approximates a single operator \mathcal{G}^\dagger , which maps a certain function u to $\mathcal{G}^\dagger(u)$.

2.3. Spatio-temporal Forecasting

Given n_s fixed spatial locations denoted by $\mathbf{X} = \{\mathbf{x}_i \in D : i = 1, \dots, n_s\}$, and n_t timestamps $\{t_j : j = 1, \dots, n_t\}$,

for the forecasting tasks, our goal is to learn a function $F(\cdot)$ as our model for approximating the true mapping of historical $n_t \times n_s$ observed physical quantities to the future $n'_t \times n_s$ quantities, that is

$$\begin{aligned} & [u(\mathbf{X}, t_1), \dots, u(\mathbf{X}, t_{n_t})] \\ \xrightarrow{F} & [u(\mathbf{X}, t_{n_t+1}), \dots, u(\mathbf{X}, t_{n_t+n'_t})]. \end{aligned} \quad (3)$$

For spatially-inductive forecasting, the learned mapping F can generalize well for any spatial location $\mathbf{x}_{\text{new}} \in D$ which are unseen to the model and not included in \mathbf{X} for training the model, i.e. $\mathbf{x}_{\text{new}} \notin \mathbf{X}$, given its previous observations $[u(\mathbf{x}_{\text{new}}, t_1), \dots, u(\mathbf{x}_{\text{new}}, t_{n_t})]$. For temporally-irregular forecasting, the quantities can be non-uniformly sampled, i.e. $t_{j+1} - t_j \neq t_j - t_{j-1}$, and for other unobserved timestamps $t \in [0, T]$, the model generalizes well.

To generalize to both continuous spatial domain D and temporal domain $[0, T]$, our method aims to directly model the internal mechanisms of system's dynamics by learning the spatio-temporal patterns according to PDEs with neural operators, rather than fit the discrete signals on spatial and temporal domains auto-regressively.

3. Proposed Methods

3.1. Graph Kernel Encoder

Since the timestamps of input observations are usually fixed, we attempt to model the spatial dependency at each time t_j in the encoder. In this way, we assume that the underlying PDE is supposed to be of the Eq. 2 formulation. Therefore, the encoder of history observations of our model can be chosen as neural-operators-based in Sec. 2.2, whose architecture at a single timestamp is given in Fig. 2.

Solution representation function. For an observed quantity $u_t(\mathbf{x}) = u(\mathbf{x}, t)$, we first lift $u(\mathbf{x}, t)$ into a higher dimensional representation space with a linear transformation to increase expressiveness, which can be written as $P(u(\mathbf{x}, t)) = v(\mathbf{x}, t) \in \mathbb{R}^d$, where $v(\cdot, \cdot) \in \mathcal{U}^d$ is defined as representation function. We assume that there exists a true solution representation function in the function space \mathcal{U}^d , and we aim to use v^{enc} for approximating it after the mapping of the encoders based on learned operator.

Graph kernel operator. To encode the history observations into representation space, we use an operator to update v_t to approximate the true solution representation function. We follow kernel operators (Li et al., 2020b;a) for parametric PDEs, which is inspired by the solution of uniformly elliptic operator and empirically proved discretization-invariant, to model the action of the integral operator written as

$$u_t(\mathbf{x}) = \mathcal{F}^\dagger(a_t)(\mathbf{x}) = \int_D G_{a_t}(\mathbf{x}, \mathbf{y}) [f(\mathbf{y}, t) + \Gamma_{a_t}(\mathbf{y})] d\mathbf{y}, \quad (4)$$

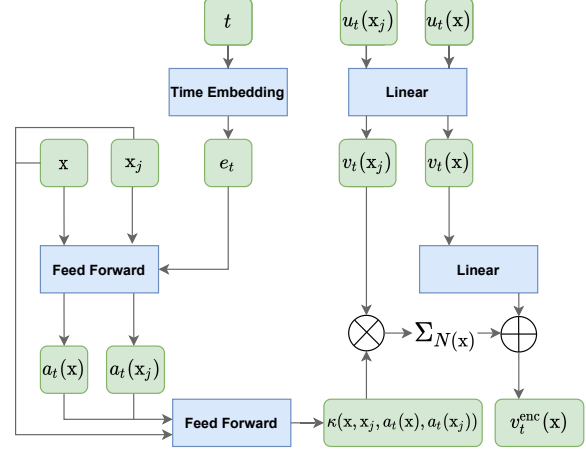


Figure 2. The workflow to update the history observations into solution representation functions. \mathbf{x}_j is in the neighborhood of \mathbf{x} . \oplus and \otimes are element-wise add and product, and $\sum_{N(\mathbf{x})}$ means the summation of \mathbf{x} 's neighborhood.

where G_{a_t} is a Newtonian potential and Γ_{a_t} is an operator defined by appropriate sums and compositions of the modified trace and co-normal derivative operators (Sauter & Schwab, 2011). Lending the Eq. 4 representing an integral operator as iterative architecture, it defines the operator $\mathcal{K}_{a_t} : \mathcal{U}^d \rightarrow \mathcal{U}^d$ as

$$(\mathcal{K}_{a_t} v_t)(\mathbf{x}) = \int_D \kappa_\phi(a_t(\mathbf{x}), a_t(\mathbf{y}), \mathbf{x}, \mathbf{y}) v_t(\mathbf{y}) d\mathbf{y}, \quad (5)$$

where κ_ϕ with learnable parameters ϕ is the kernel function taking spatial locations (\mathbf{x}, \mathbf{y}) and values of parametric function $(a_t(\mathbf{x}), a_t(\mathbf{y}))$ as its inputs. As such, the corresponding update approximation which mimics the message passing neural network (Gilmer et al., 2017) is obtained by

$$\begin{aligned} v_t^{\text{enc}}(\mathbf{x}) &= (\mathcal{K}_{a_t} v_t)(\mathbf{x}) \\ &\approx \sigma \left(W v_t(\mathbf{x}) + \frac{1}{|N(\mathbf{x})|} \sum_{\mathbf{x}_j \in N(\mathbf{x})} \kappa_\phi(a_t(\mathbf{x}), a_t(\mathbf{x}_j), \mathbf{x}, \mathbf{x}_j) v_t(\mathbf{x}_j) \right), \end{aligned} \quad (6)$$

where $W \in \mathbb{R}^{d \times d}$ is learnable weights, and $N(\mathbf{x})$ is the neighborhood of \mathbf{x} , which is established by an ϵ -ball algorithm (See Appendix A.2.). In specific, we formulate κ_ϕ as a feed-forward neural network. By using the proposed multipole graph kernel network, the updating steps are able to capture the long-range spatial dependency between points (Ying et al., 2004; Li et al., 2020a) as well as handle the signals with *spatially-inductive* and *temporally-irregularly forecasting*: When an observation $u_t(\mathbf{x}_{\text{new}})$ on an unseen spatial point \mathbf{x}_{new} is obtained, the $v_t^{\text{enc}}(\mathbf{x}_{\text{new}})$ can be inductively obtained according to Eq. 6 as long as its neighborhood $N(\mathbf{x}_{\text{new}})$ is known. Moreover, for any input u_t , we can always obtain v_t^{enc} regardless of non-uniform intervals between timestamps.

Parametric function formulation. For classical PDE models which the kernel operators try to solve, the parametric functions are known. In contrast, the parametric functions are unknown in spatio-temporal forecasting tasks. Thus, we need to approximate $a_t(\mathbf{x})$ parameterized by timestamps t and taking location \mathbf{x} as its input. We first employ trigonometric transformation based on positional encodings used in transformer language models (Vaswani et al., 2017) to embed timestamps into d_t -dimensional space.

$$\mathbf{e}_t = [\sin(\omega_1 t), \cos(\omega_1 t), \dots, \sin(\omega_{d_t} t), \cos(\omega_{d_t} t)], \quad (7)$$

where $\{\omega_k\}_{1 \leq k \leq d_t}$ are learnable parameters, and t can be a vector containing time features, such as year, month, day and hour. Then, the parametric function is formulated as a feed-forward network taking the concatenation of time embeddings and locations as inputs, i.e. $a_t(\mathbf{x}) = \text{MLP}([\mathbf{x}, \mathbf{e}_t])$.

3.2. Deep Operator Decoder

In the decoder which is used to generate future predictions given the past representation functions, the values of physical quantities of ground-truth are not given in the prediction process. Therefore, we cannot firstly lift $u(\mathbf{x}, t)$ into the representation space for updating. To address it, combined Eq. 1 and Eq. 2, we write the PDE as

$$\frac{\partial u(\mathbf{x}, t)}{\partial t} = (\mathcal{L}_{a_t} u_t)(\mathbf{x}) = f(\mathbf{x}, t), \quad (8)$$

which implies $u(\mathbf{x}, t) = \int_0^t f(\mathbf{x}, \tau) d\tau = (\mathcal{G}u)(\mathbf{x}, t)$. Let $\mathcal{I}(f)(\mathbf{x}, t) = \int_0^t f(\mathbf{x}, \tau) d\tau$, where $\mathcal{I} : \mathcal{U} \rightarrow \mathbb{R}$ is the integral operator, and the construction of \mathcal{G} is shown in Fig. 3.

$$\begin{array}{ccccc} u^{\text{enc}} & \xrightarrow{\mathcal{L}_{a_t}} & f & \xrightarrow{\mathcal{I}} & u^{\text{dec}} \\ & \downarrow & \downarrow & & \uparrow \\ & & \mathcal{G} & & \end{array}$$

Figure 3. The construction of $\mathcal{G} = \mathcal{I} \circ \mathcal{L}_{a_t}$. To differentiate the solution function fed in the encoder and generated by the decoder, we use u^{enc} and u^{dec} to denote them.

Inspired by this, we try to use \mathcal{G}^\dagger to approximate \mathcal{G} , to obtain the representation function solution as

$$v^{\text{dec}}(\mathbf{x}, t) \approx (\mathcal{G}^\dagger v^{\text{enc}})(\mathbf{x}, t).$$

Universal approximation for operator. Following the Universal Operators in Sec. 2.2, we formulate \mathcal{G}^\dagger according to the theorem below.

Theorem 1. (Universal Approximation Theorem for Operator) (Chen & Chen, 1995) Suppose that σ is a continuous non-polynomial function, D is a Banach Space, $D_1 \in D, D_2 \in \mathbb{R}^M$ are two compact sets in D and \mathbb{R}^M , respectively, V is a compact set in $C(D_1)$, and \mathcal{G} is a nonlinear continuous operator, which maps V

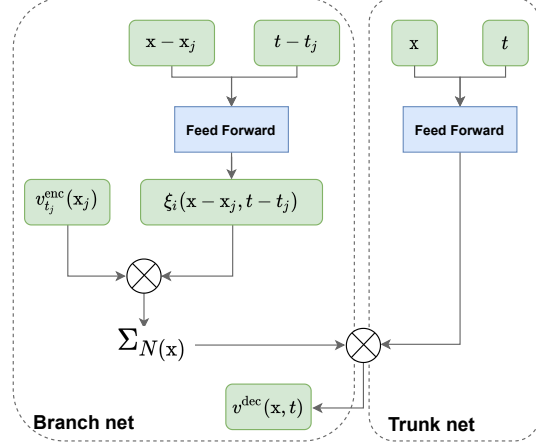


Figure 4. The workflow to approximate the solution representation functions for future prediction using past representations. \mathbf{x}_j is in the neighborhood of \mathbf{x} .

into $C(D_2)$. For any $\epsilon > 0$, there are positive integers s, n, r , constants $c_i^k, \xi_{ij}^k, \theta_i^k, \zeta_k \in \mathbb{R}$, $\eta_k \in \mathbb{R}^m$, $\mathbf{p}_j \in D_1$, $i = 1, \dots, s; j = 1, \dots, n; k = 1, \dots, r$, such that

$$|\mathcal{G}(u)(\mathbf{q}) - \mathcal{G}^\dagger(u)(\mathbf{q})| < \epsilon, \quad (9)$$

where

$$\mathcal{G}^\dagger(u)(\mathbf{q}) = \sum_{k=1}^r \sum_{i=1}^s c_i^k \sigma \left(\sum_{j=1}^n \xi_{ij}^k u(\mathbf{p}_j) + \theta_i^k \right) \sigma(\eta_k \mathbf{q} + \zeta_k)$$

holds for all $u \in V$ and $\mathbf{q} \in D_2$.

This approximation theorem indicates the potential application of neural networks to learn nonlinear operators from data. Thereby, we let $\mathbf{p}_j \in \{(\mathbf{x}_j, t_j) : j = 1, \dots, n_s \times n_t\}$, and $M = m + 1$. For each future timestamp $t > t_{n_t}$ for prediction, we write its representation solution function as

$$\begin{aligned} v_k^{\text{dec}}(\mathbf{x}, t) \\ = \sum_{i=1}^d c_i^k \sigma \left(\sum_{j=1}^{n_s \times n_t} \xi_{ij}^k v_{t_j}^{\text{enc}}(\mathbf{x}_j) + \theta_i^k \right) \sigma(\eta_k[\mathbf{x}, t] + \zeta_k), \end{aligned} \quad (10)$$

where $v_{t_j}^{\text{enc}}(\mathbf{x}_j), \xi_{ij}^k, \eta_k \in \mathbb{R}^d$, $c_i^k, \theta_i^k, \zeta_k \in \mathbb{R}$ and $v_k^{\text{dec}}(\mathbf{x}, t)$ is the k -th component of $v^{\text{dec}}(\mathbf{x}, t) \in \mathbb{R}^d$. Following DEEPONET (Lu et al., 2021), we first put the target points (\mathbf{x}, t) into a feed-forward network called Trunk net,

$$\text{MLP}_{ik}^{\text{Tr}}(\mathbf{x}, t) = \sigma(\eta_k[\mathbf{x}, t] + \zeta_k), \quad (11)$$

and put all the obtained past representations $\{v_{t_j}^{\text{enc}}(\mathbf{x}_j)\}$ into the other network called Branch net, as

$$\text{MLP}_{ik}^{\text{Br}}(\mathbf{x}_j, t_j) = \sigma \left(\sum_{j=1}^{n_s \times n_t} \xi_{ij}^k v_{t_j}^{\text{enc}}(\mathbf{x}_j) + \theta_i^k \right). \quad (12)$$

By multiplying the two outputs of $\text{MLP}^{\text{Tr}}(\mathbf{x}, t)$ and $\text{MLP}^{\text{Br}}(\mathbf{x}, t)$ with a linear transformation whose parameter is $\{c_i^k\}$ stacked after, we obtain the representation function $v^{\text{dec}}(\mathbf{x}, t) = (v_1^{\text{dec}}(\mathbf{x}, t), \dots, v_d^{\text{dec}}(\mathbf{x}, t))$ for prediction.

Revised flexible decoder. The construction of the Branch-Trunk decoder according to Eq. 10 is time-continuous, so it is able to solve the *temporally-irregular forecasting* theoretically. However, this establishment does not allow inductive forecasting. The reason for it is that:

When a sequence of observations on an unseen spatial point \mathbf{x}_{new} is obtained, the Branch Net in Eq. 12 of the decoder does not permit $\{v_{t_j}^{\text{enc}}(\mathbf{x}_{\text{new}})\}$ which is inductively obtained by the encoder to be added to $\{v_{t_j}^{\text{enc}}(\mathbf{X})\}$ to compute $\{v^{\text{dec}}(\mathbf{x}_{\text{new}}, t)\}$, because the number of parameter $\{\xi_{ij}^k\}$ for index j is fixed as $n_s \times n_t$, which is inextensible.

To address it, we revise the Branch net as

$$\begin{aligned} & \text{AGG}_{ik}^{\text{Br}}(\mathbf{x}, \mathbf{x}_j, t, t_j) \quad (13) \\ &= \sigma \left(\frac{1}{|N(\mathbf{x})|} \sum_{\substack{\mathbf{x}_j \in N(\mathbf{x}) \\ 1 \leq j \leq n_s \times n_t}} \xi_i^k(\mathbf{x} - \mathbf{x}_j, t - t_j) v_{t_j}^{\text{enc}}(\mathbf{x}_j) + \theta_i^k \right). \end{aligned}$$

We use ‘ AGG^{Br} ’ to denote the revised Branch net, which means that the representation functions are updated by aggregating messages from their neighbors’ previous representation functions, where the message-passing weights are inductively obtained by a feed-forward network $\xi_i^k(\cdot, \cdot)$ with relative spatial location and time as inputs. Fig. 4 gives the workflows of our decoder model. In this way, when a sequence of history observations is added, the Branch’s output can still be flexibly obtained as long as the neighborhood is known.

In addition, an auxiliary advantage brought by Eq. 13 is that the potential explosion of model’s parameter number can be avoided. In Eq. 12, when the number of observed points are large, the computational complexity may explore. As n_s increases by 1, the parameter number will increase by $\mathcal{O}(n_t \times d \times d)$, complexity of which may be unaffordable. The revised decoder’s parameter number will not change as the number of spatial sample points increases.

3.3. Loss function

For training, after getting $\{v_t^{\text{enc}}(\mathbf{X}) : t = t_1, \dots, t_{n_t}\}$ as the values of representation function obtained by encoder, and $\{v_t^{\text{dec}}(\mathbf{X}, t) : t = t_{n_t+1}, \dots, t_{n_t+n'_t}\}$ as the values of representation function obtained by decoder, where $\mathbf{X} = \{\mathbf{x}_i \in D : i = 1, \dots, n_s\}$ are the spatial locations of sample points as shown in Sec. 2.3, we use a linear projector P' to map them back to \mathcal{U} , and use mean absolute error (MAE) to construct the loss function, which reads

$$\begin{aligned} L = & \frac{\alpha}{n_t n_s} \sum_{t=t_1}^{t_{n_t}} \|P'(v_t^{\text{enc}}(\mathbf{X})) - u(\mathbf{X}, t)\|_1 \quad (14) \\ & + \frac{1}{n'_t n_s} \sum_{t=t_{n_t+1}}^{t_{n_t+n'_t}} \|P'(v_t^{\text{dec}}(\mathbf{X})) - u(\mathbf{X}, t)\|_1, \end{aligned}$$

where the first term we call the reconstruction loss, to restrict the encoder and projector to preserve information from inputs, with α ‘*the weight of reconstruction loss*’, and the second term we call the prediction loss, to evaluate the prediction performance of the model.

4. Related Works

Graph Spatio-temporal networks. Spatio-temporal forecasting networks are mostly graph-based thanks to their ability to learn representations of spatially-irregular distributed signals, such as traffic flows recorded by sensors (Yu et al., 2018; Li et al., 2018; Guo et al., 2019b; Bai et al., 2020; Zhao et al., 2020; Li et al., 2021a). These works usually regard signals’ location as nodes, and establish graphs to describe the nodes’ dependency according to their spatial distance. Also, some works learn the adjacency relations of nodes without the prior graph structure, by using attention mechanisms (Yu et al., 2018; Li et al., 2018; Zhao et al., 2020), graph structure learning techniques (Shang et al., 2021), node embeddings (Bai et al., 2020) and so on. However, these methods are constructed for transductive tasks on discrete nodes. Recently, a spatio-temporal meteorological forecasting methods for physical quantities located on continuous space (earth sphere) is proposed (Lin et al., 2021), but it still aims to ‘fit’ the signals on discrete nodes. In comparison, our model aims to both handle irregularly distributed signals and allow spatially-inductive forecasting by employing multipole graph neural operators (Li et al., 2020a).

PDE-driven spatio-temporal networks. An increasing number of works combining spatio-temporal networks with differential equations have been produced in recent years. A series of them are established for data with regular grids, such as videos (Guen & Thome, 2020; Donà et al., 2021). These methods are usually constructed on (2D-image-)convolution neural networks as the basic architecture of spatial encoders, while our model aims to handle spatially-irregular distributed points, and thus is graph-based. Another stream of PDE-driven networks follow Neural ODE (Chen et al., 2019) for modeling dynamical systems (Çağatay Yıldız et al., 2019; Rubanova et al., 2019). Because of the high computational cost of integral estimation and backward propagation, these models are not feasible for long-term forecasting. We also establish a version of ODE-based model (Appendix B.) and conduct experiment illustrating its infeasible time cost.

Neural operators. A line of neural networks have been designed to model one specific instance of the PDEs (E & Yu, 2017; Bar & Sochen, 2019; Smith et al., 2020; Pan & Duraisamy, 2020; Raissi et al., 2020) with prior physical knowledge. For example, structural priors and constraints

are combined for fluid prediction (Tompson et al., 2017; Raissi et al., 2020), and Hamiltonian mechanics are used to construct non-regression losses (Greydanus et al., 2019; Chen et al., 2020; Toth et al., 2020) to learn basic laws of physics. In contrast, our model aims to be applicable to general spatio-temporal forecasting. Thus, we turn to neural operators (Lu et al., 2021; Bhattacharya et al., 2021; Li et al., 2020a; 2021b; Nelsen & Stuart, 2021) for solutions, which require no knowledge of the underlying PDE, only data. Besides, their learned network parameters can be generalized with different discretizations of points. In this way, we conjecture the operator can capture the implicit mechanisms of the dynamics, and thus employ it as the spatial fundamental modules of our model.

5. Experiments

In the experiment part, we aim to figure out the following three questions:

- Q.1** How the proposed STONET performs: Does it achieve improved performance on forecasting tasks of continuous spatial domain, compared with other graph-based spatio-temporal neural networks?
- Q.2** Whether STONET allows spatially-inductive forecasting: Does the trained model achieve comparable accuracy of prediction on unseen spatial points, given their previous observations?
- Q.3** Whether STONET allows temporally-irregular forecasting: Does the model give accurate predictions, even when the labels of future predictions are sampled irregularly, or missing with a ratio?

5.1. Experiment Setup

Protocol. Because our method is graph-based to handle the spatially-irregular signals or physical quantities, we choose 8 methods which are all graph-based spatio-temporal models for performance comparison. Table. 1 and Appendix C.1. give descriptions of the methods, where ‘*Spatial*’ and ‘*Temporal*’ represent the modules to capture spatial dependency and temporal dynamics. Our conclusion is based on the implementation of TORCH-GEOMTEMP (Rozemberczki et al., 2021) and each methods’ open source code. Three widely used metrics - Mean Absolute Error (MAE), Root Mean Square Error (RMSE), and Mean Absolute Percentage Error (MAPE) are deployed to measure the performance. The reported mean and standard deviation of metrics are obtain through 5 independent experiments with different random seeds. All the models for comparison are trained with target function of MAE and optimized by Adam optimizer. The hyper-parameters are chosen through a carefully tuning on the validation set. In implementation, we stack several decoders for different terms of forecasting in STONET as analyzed in Sec. 5.5 and Appendix C.5.

Table 1. Comparison of different spatio-temporal methods

Methods	Spatial	Temporal
TGCN (Zhao et al., 2020)	Vanilla GCN (Kipf & Welling, 2017)	GRU
STGCN (Yu et al., 2018)	Vanilla GCN (Kipf & Welling, 2017)	1D Conv
MSTGCN (Guo et al., 2019a)	ChebConv (Defferrard et al., 2017)	1D Conv
ASTGCN (Guo et al., 2019a)	GAT (Veličković et al., 2018)	Attention
GCGRU (Seo et al., 2016)	ChebConv (Defferrard et al., 2017)	GRU
DCRNN (Li et al., 2018)	DiffConv (Atwood & Towsley, 2016)	GRU
AGCRN (Bai et al., 2020)	Node Similarity (Bai et al., 2020)	GRU
CLCRN (Lin et al., 2021)	CondLocalConv (Lin et al., 2021)	GRU

Dataset. We conduct an evaluation on 6 datasets, whose forecasting target signals are all spatially-continuous physical quantities, including Wave (Saha et al., 2021), Solar energy (Lai et al., 2018), Temperature, Humidity, Cloud cover and Wind component (Rasp et al., 2020). All the evaluation tasks are 12-to-12 auto-regressive forecasting, where the input and forecasting sequence length are all set as 12. The spatial domain includes both 2D plane and 2D sphere (earth’s surface). Dataset descriptions are shown in Table. 2. For CLCRN (Lin et al., 2021), it is established for dataset whose spatial domain is sphere, so we do not compare its performance on planar dataset. To differentiate from the time point, we call the fixed spatial points as nodes, because all the methods are graph-based.

Table 2. Dataset description

Datasets	Wave	Solar Energy	Temperature
Spatial domain	2D plane	2D plane	2D sphere
Dimension	1	1	1
# of nodes	512	137	2048
Granularity	0.001s	5 min	1h
Datasets	Humidity	Cloud cover	Wind component
Spatial domain	2D sphere	2D sphere	2D sphere
Dimension	1	1	2
# of nodes	2048	2048	2048
Granularity	1h	1h	1h

5.2. Performance Comparison

We first conduct experiments on the datasets with 8 baselines and our STONET. Because MAPE is of great difference among methods and hard to agree on an order of magnitude due to its incompatible units, we show it in Appendix C.2.

From Table. 3, it can be concluded that

- Due to the high expressivity of STONET, it outperforms other models for comparison with a large margin on all but the smallest of the benchmark datasets such as Cloud Cover.
- Because most of the compared methods are established for traffic forecasting on discrete nodes, they show a decrease in performance for continuous physical quantity forecasting tasks. The difference between two tasks is analyzed in previous works (Lin et al., 2021).

Table 3. Forecasting results on different datasets. Results in **bold** are the top-1 performance, and results with underlines are the second. ‘Improvements’ is the percentage of top-1 over the second.

	MAE	RMSE	MAE	RMSE	MAE	RMSE	
	Wave ($\times 10^{-4}$)	Solar Energy (mw)	Temperature (k)				
TGCN	3.7619 \pm 0.0144	5.8999 \pm 0.0485	2.0036 \pm 0.0423	4.6218 \pm 0.3820	3.8638 \pm 0.0970	5.8554 \pm 0.1432	
STGCN	4.1202 \pm 0.1800	6.4805 \pm 0.4165	1.4048 \pm 0.0184	4.1451 \pm 0.0249	4.3525 \pm 1.0442	6.8600 \pm 1.1233	
MSTGCN	6.0639 \pm 0.2664	7.8891 \pm 0.5628	1.9224 \pm 0.0251	4.0406 \pm 0.0471	1.2199 \pm 0.0058	1.9203 \pm 0.0093	
ASTGCN	5.3150 \pm 0.2012	7.1699 \pm 0.2045	1.9834 \pm 0.0054	4.1312 \pm 0.0095	1.4896 \pm 0.0130	2.4622 \pm 0.0023	
GCGRU	3.5617 \pm 0.4817	5.6927 \pm 0.4181	1.0661 \pm 0.0867	2.6303 \pm 0.1197	1.3256 \pm 0.1499	2.1721 \pm 0.1945	
DCRNN	3.7338 \pm 0.1167	5.8157 \pm 0.0859	1.1031 \pm 0.1140	2.7474 \pm 0.2229	1.3232 \pm 0.0864	2.1874 \pm 0.1227	
AGCRN	4.2048 \pm 0.1161	6.1559 \pm 0.0776	1.1845 \pm 0.0902	2.6823 \pm 0.1261	1.2551 \pm 0.0080	1.9314 \pm 0.0219	
CLCRN	-	-	-	-	1.1688 \pm 0.0457	1.8825 \pm 0.1509	
STONET	3.1959\pm0.0722	5.2201\pm0.0743	0.8699\pm0.0399	2.1533\pm0.0563	0.8972\pm0.0230	1.4963\pm0.0422	
Improvements	10.2703%	8.3019%	18.4035%	18.1348%	23.2375%	20.5153%	
	Humidity (% $\times 10$)		Cloud Cover (% $\times 10^{-1}$)	Wind Component (ms $^{-1}$)			
	TGCN	1.4700 \pm 0.0295	2.1066 \pm 0.0551	2.3934 \pm 0.0216	3.6512 \pm 0.0223	4.1747 \pm 0.0324	5.6730 \pm 0.0412
	STGCN	0.7975 \pm 0.2378	1.1109 \pm 0.2913	2.0197 \pm 0.0392	2.9542 \pm 0.0542	3.6477 \pm 0.0000	4.8146 \pm 0.0003
	MSTGCN	0.6093 \pm 0.0012	0.8684 \pm 0.0019	1.8732 \pm 0.0010	2.8629 \pm 0.0073	1.9440 \pm 0.0150	2.9111 \pm 0.0292
	ASTGCN	0.7288 \pm 0.0229	1.0471 \pm 0.0402	1.9936 \pm 0.0002	2.9576 \pm 0.0007	2.0889 \pm 0.0006	3.1356 \pm 0.0012
	GCGRU	0.5007 \pm 0.0002	0.7891 \pm 0.0006	1.5925 \pm 0.0023	2.5576 \pm 0.0116	1.4116 \pm 0.0057	2.2931 \pm 0.0047
	DCRNN	0.5046 \pm 0.0011	0.7956 \pm 0.0033	1.5938 \pm 0.0021	2.5412 \pm 0.0044	1.4321 \pm 0.0019	2.3364 \pm 0.0055
	AGCRN	0.5759 \pm 0.1632	0.8549 \pm 0.2025	1.7501 \pm 0.1467	2.7585 \pm 0.1694	2.4194 \pm 0.1149	3.4171 \pm 0.1127
	CLCRN	0.4531 \pm 0.0065	0.7078 \pm 0.0146	1.4906\pm0.0037	<u>2.4559\pm0.0027</u>	<u>1.3260\pm0.0483</u>	<u>2.1292\pm0.0733</u>
STONET	0.4273\pm0.0256	0.6584\pm0.0287	1.4933\pm0.0030	2.4142\pm0.0016	1.2192\pm0.0064	1.9774\pm0.0122	
Improvements	5.6841%	6.9794%	-0.1811%	1.7794%	8.0543%	7.1294%	

5.3. Spatially Inductive Evaluation

The second part is to figure out **Q.2** : whether the proposed STONET allows *spatially-inductive forecasting*. We preprocess the datasets to ensure that there are unseen the spatial nodes in the datasets for models to be trained with. For example, for the four weather datasets, we first downsample the resolution to 16×32 , with 512 nodes used for training, and randomly choose another 512 different nodes for inductive evaluation. Other details on preprocessing datasets for this task are described in Appendix C.3.

Our results of performance on original nodes (for transductive forecasting) and unseen nodes (for inductive forecasting) are shown in Table 4, where ‘Deviation’ is calculated by $100\% \times \frac{\text{MAE}_{\text{ind}} - \text{MAE}_{\text{tran}}}{\text{MAE}_{\text{tran}}}$. Fig. 5 shows the performance of inductive tasks on unseen nodes with different ratios, where $\text{Ratio} = \frac{\#\{\text{unseen node}\}}{\#\{\text{original node}\}}$, on several datasets. Results on other datasets are in Appendix C.3. We conclude that

- The overall performance on transductive tasks shows decrease except in Wave, because downsampling is conducted in the other five datasets, causing the loss of spatial information.
- The evaluation on unseen nodes usually shows a tiny decrease compared with the nodes for training, but still achieves a competitive accuracy with the ‘Deviation’ less than 4%.
- As the ratio of unseen points increases, the performance on them usually shows a trend of decrease with some fluctuation. An explanation of it is that

Table 4. Evaluation results on transductive and inductive tasks.

Metric	Tasks	Wave	Solar Energy	Temperature
MAE	Trans.	3.1959 \pm 0.0722	1.1448 \pm 0.0206	0.9344 \pm 0.0252
	Induc.	3.1719 \pm 0.3624	1.1799 \pm 0.0373	0.9638 \pm 0.0371
RMSE	Trans.	5.2586 \pm 0.0743	2.4654 \pm 0.0454	1.5250 \pm 0.0455
	Induc.	5.3794 \pm 0.2933	2.5028 \pm 0.0427	1.5631 \pm 0.0594
Deviation		-0.7509%	+3.0660%	+3.1464%
Metric	Tasks	Humidity	Cloud Cover	Wind Component
MAE	Trans.	0.4678 \pm 0.0167	1.5874 \pm 0.0028	1.3124 \pm 0.0149
	Induc.	0.4847 \pm 0.0248	1.6024 \pm 0.0101	1.3330 \pm 0.0154
RMSE	Trans.	0.7075 \pm 0.0150	2.5223 \pm 0.0039	2.1588 \pm 0.0375
	Induc.	0.7398 \pm 0.0132	2.5213 \pm 0.0183	2.1459 \pm 0.0462
Deviation		+3.6082%	+0.9449%	+1.5696%

the message-passing patterns of STONET entangle intricately, and could possibly be disturbed when a large number of unseen nodes are included for forecasting.

To sum up, empirical studies illustrate that the inductive forecasting task can be well-solved by our model when the number of unseen nodes is not extremely large, since the deviation is smaller than 4% in different *Ratios*.

5.4. Temporally Irregular Evaluation

To demonstrate that our model can solve the **Q.3**, we conduct experiments in one of the *temporally-irregular forecasting* scenarios – data with missing values, since all the evaluated datasets are all uniformly sampled in temporal domains. In detail, the previous setting is all based on a n_t -to- n'_t forecasting task, where $n_t = n'_t = 12$, while in this part, we ran-

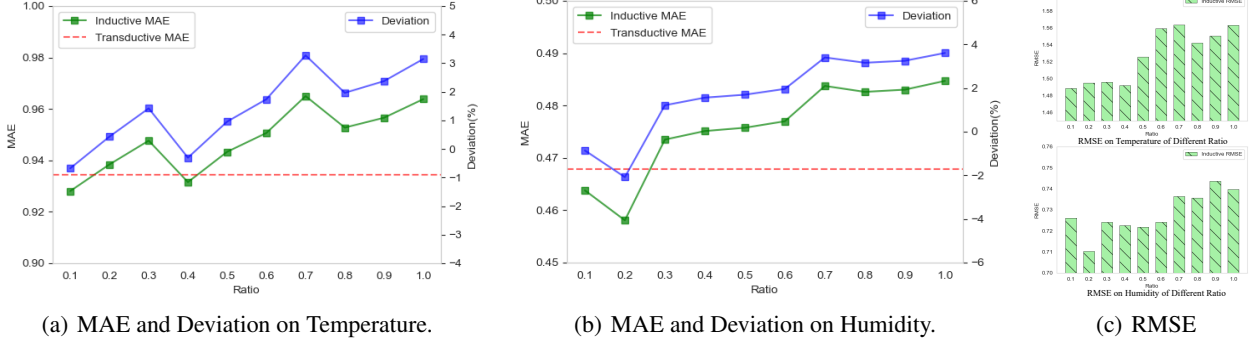


Figure 5. The change of MAE, Deviation and RMSE on different ratio of inductive nodes number on Dataset of Humidity and Temperature. For other results, see Appendix C.3.

domly remove labels of different sequences of data at different timestamps with a ratio, leading to the non-uniformity of time-interval. We set $n_{t'} = \#\{\text{output timestamps}\}$, where $n_{t'} \leq 12$. For example, if we randomly remove spatial snapshots at 2 timestamps, we think that it is equivalent to the missing data scenario where the missing ratio equals $\frac{2}{12}$, and $n_{t'} = 10$.

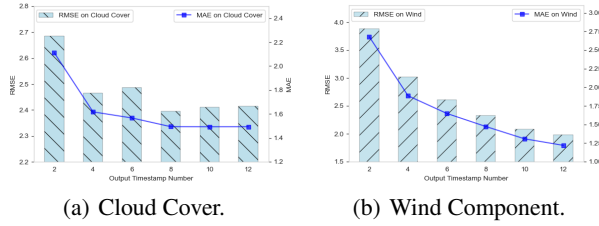


Figure 6. The change of MAE and RMSE on different output timestamp numbers ($n_{t'}$) on Dataset of Cloud Cover and Wind Component. For other results, see Appendix C.4.

Fig. 6 shows the performance change of different $n_{t'}$. Intuitively, when the $n_{t'}$ is extremely small, e.g. $n_{t'} = 2$ and missing ratio equals $\frac{5}{6}$, the performance demonstrates a dramatical decrease, due to a massive loss of supervised labels. In comparison, when the missing ratio is small, e.g. $n_{t'} = 10$, the performance is comparable. Therefore, even if STONET has the ability to handle the temporally-irregular forecasting tasks, a large ratio of missing data in the temporal domain compromises the model performance.

5.5. Further Ablation Study

Several hyper-parameters affect the model performance, and in this part we try to explore their impacts. First, we aim to figure out how the ‘embedding size’ i.e. d , and the ‘layer number’ determine the expressivity of the model. Second, as demonstrated in (Li et al., 2020a), the multi-leveled graphs in multipole graph neural network encoder help to increase the accuracy, because it enables each node to aggregate messages from farther nodes in spatial domains.

Thus, we attempt to figure out its effects. Note that when the ‘number of levels’ of multipole graphs equals 1, the graph kernel encoder in STONET is the same as proposed in (Simonovsky & Komodakis, 2017). Finally, we conduct analysis on α , the ‘weight of the reconstruction loss’. We give results on Solar Energy and Temperature, and the results on other datasets are shown in Appendix C.5.

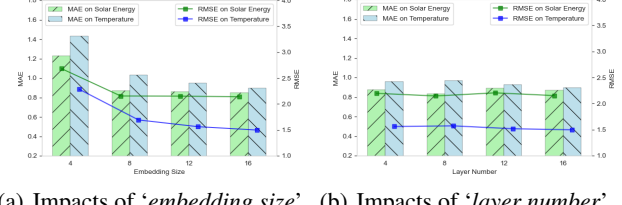


Figure 7. The change of MAE and RMSE on different hyper-parameters on Dataset of Solar Energy and Temperature.

Table 5. Comparison on different ‘number of levels’ and ‘loss weight’ on Dataset of Solar Energy and Temperature.

Datasets	Solar Energy		Temperature		
	# of levels	MAE	RMSE	MAE	RMSE
1	1.0630 \pm 0.0359	2.5188 \pm 0.0490	0.8917 \pm 0.0164	1.4825 \pm 0.0423	
2	0.9729 \pm 0.2378	2.3364 \pm 0.2913	0.8718 \pm 0.0302	1.4311 \pm 0.0571	
3	0.8699 \pm 0.0207	2.1533 \pm 0.0305	0.8972 \pm 0.0230	1.4963 \pm 0.0422	
Datasets	Solar Energy		Temperature		
	loss weight	MAE	RMSE	MAE	RMSE
0.0	0.9195 \pm 0.0102	2.1677 \pm 0.0209	0.8845 \pm 0.0196	1.4837 \pm 0.0313	
0.5	0.8699 \pm 0.0399	2.1533 \pm 0.0563	0.8972 \pm 0.0230	1.4963 \pm 0.0422	
1.0	0.9159 \pm 0.0430	2.1724 \pm 0.0625	0.9692 \pm 0.0216	1.5880 \pm 0.0392	

6. Conclusion

An operator-driven spatio-temporal forecasting network is proposed, with its encoder based on graph kernel operator and decoder based on universal operator. Experiments show that it achieves improved performance in continuous physical quantities forecasting on spatial points of *spatially-irregular distribution*, and allows both *spatially-inductive* and *temporally-irregular forecasting*.

References

Antman, S. S. Nonlinear problems of elasticity. 2005.

Atwood, J. and Towsley, D. Diffusion-convolutional neural networks, 2016.

Bai, L., Yao, L., Li, C., Wang, X., and Wang, C. Adaptive graph convolutional recurrent network for traffic forecasting, 2020.

Bar, L. and Sochen, N. Unsupervised deep learning algorithm for pde-based forward and inverse problems, 2019.

BearM, J. and Corapcioglu, Y. Physics-informed probabilistic learning of linear embeddings of nonlinear dynamics with guaranteed stability. 2012.

Bhattacharya, K., Hosseini, B., Kovachki, N. B., and Stuart, A. M. Model reduction and neural networks for parametric pdes, 2021.

Chen, R. T. Q., Rubanova, Y., Bettencourt, J., and Duvenaud, D. Neural ordinary differential equations, 2019.

Chen, T. and Chen, H. Universal approximation to nonlinear operators by neural networks with arbitrary activation functions and its application to dynamical systems. *IEEE Transactions on Neural Networks*, 6(4):911–917, 1995. doi: 10.1109/72.392253.

Chen, Z., Zhang, J., Arjovsky, M., and Bottou, L. Symplectic recurrent neural networks, 2020.

Defferrard, M., Bresson, X., and Vandergheynst, P. Convolutional neural networks on graphs with fast localized spectral filtering, 2017.

Donà, J., Franceschi, J.-Y., Lamprier, S., and Gallinari, P. Pde-driven spatiotemporal disentanglement, 2021.

E, W. and Yu, B. The deep ritz method: A deep learning-based numerical algorithm for solving variational problems, 2017.

Gilmer, J., Schoenholz, S. S., Riley, P. F., Vinyals, O., and Dahl, G. E. Neural message passing for quantum chemistry, 2017.

Greenfeld, D., Galun, M., Kimmel, R., Yavneh, I., and Basri, R. Learning to optimize multigrid pde solvers, 2019.

Greydanus, S., Dzamba, M., and Yosinski, J. Hamiltonian neural networks, 2019.

Guen, V. L. and Thome, N. Disentangling physical dynamics from unknown factors for unsupervised video prediction, 2020.

Guo, S., Lin, Y., Feng, N., Song, C., and Wan, H. Attention based spatial-temporal graph convolutional networks for traffic flow forecasting. *Proceedings of the AAAI Conference on Artificial Intelligence*, 33 (01):922–929, Jul. 2019a. doi: 10.1609/aaai.v33i01.3301922. URL <https://ojs.aaai.org/index.php/AAAI/article/view/3881>.

Guo, S., Lin, Y., Feng, N., Song, C., and Wan, H. Attention based spatial-temporal graph convolutional networks for traffic flow forecasting. In *Proceedings of the AAAI Conference on Artificial Intelligence*, volume 33, pp. 922–929, 2019b.

Jiang, C. M., Esmaeilzadeh, S., Azizzadenesheli, K., Kashinath, K., Mustafa, M., Tchelepi, H. A., Marcus, P., Prabhat, and Anandkumar, A. Meshfreeflownet: A physics-constrained deep continuous space-time super-resolution framework, 2020.

Kipf, T. N. and Welling, M. Semi-supervised classification with graph convolutional networks, 2017.

Kochkov, D., Smith, J. A., Alieva, A., Wang, Q., Brenner, M. P., and Hoyer, S. Machine learning accelerated computational fluid dynamics, 2021.

Lai, G., Chang, W.-C., Yang, Y., and Liu, H. Modeling long- and short-term temporal patterns with deep neural networks, 2018.

Li, F., Feng, J., Yan, H., Jin, G., Jin, D., and Li, Y. Dynamic graph convolutional recurrent network for traffic prediction: Benchmark and solution, 2021a.

Li, Y., Yu, R., Shahabi, C., and Liu, Y. Diffusion convolutional recurrent neural network: Data-driven traffic forecasting, 2018.

Li, Z., Kovachki, N., Azizzadenesheli, K., Liu, B., Bhattacharya, K., Stuart, A., and Anandkumar, A. Multipole graph neural operator for parametric partial differential equations, 2020a.

Li, Z., Kovachki, N., Azizzadenesheli, K., Liu, B., Bhattacharya, K., Stuart, A., and Anandkumar, A. Neural operator: Graph kernel network for partial differential equations, 2020b.

Li, Z., Kovachki, N., Azizzadenesheli, K., Liu, B., Bhattacharya, K., Stuart, A., and Anandkumar, A. Fundamentals of transport phenomena in porous media, 2021b.

Lin, H., Gao, Z., Xu, Y., Wu, L., Li, L., and Li, S. Z. Conditional local convolution for spatio-temporal meteorological forecasting, 2021.

Lu, L., Jin, P., Pang, G., Zhang, Z., and Karniadakis, G. E. Learning nonlinear operators via deeponet based on the universal approximation theorem of operators. *Nature Machine Intelligence*, 3:218–229, 2021.

Nelsen, N. H. and Stuart, A. M. The random feature model for input-output maps between banach spaces, 2021.

Pan, S. and Duraisamy, K. Physics-informed probabilistic learning of linear embeddings of nonlinear dynamics with guaranteed stability. *SIAM Journal on Applied Dynamical Systems*, 19(1):480–509, Jan 2020. ISSN 1536-0040. doi: 10.1137/19m1267246. URL <http://dx.doi.org/10.1137/19M1267246>.

Raissi, M., Perdikaris, P., and Karniadakis, G. Physics-informed neural networks: A deep learning framework for solving forward and inverse problems involving nonlinear partial differential equations. *Journal of Computational Physics*, 378:686–707, 2019. ISSN 0021-9991. doi: <https://doi.org/10.1016/j.jcp.2018.10.045>. URL <https://www.sciencedirect.com/science/article/pii/S0021999118307125>.

Raissi, M., Yazdani, A., and Karniadakis, G. E. Hidden fluid mechanics: Learning velocity and pressure fields from flow visualizations. *Science*, 367(6481):1026–1030, 2020.

Rasp, S., Dueben, P. D., Scher, S., Weyn, J. A., Mouatadid, S., and Thuerey, N. Weatherbench: A benchmark dataset for data-driven weather forecasting, 2020.

Rozemberczki, B., Scherer, P., He, Y., Panagopoulos, G., Riedel, A., Astefanoaei, M., Kiss, O., Beres, F., Lopez, G., Collignon, N., and Sarkar, R. Pytorch geometric temporal: Spatiotemporal signal processing with neural machine learning models, 2021.

Rubanova, Y., Chen, R. T. Q., and Duvenaud, D. Latent odes for irregularly-sampled time series, 2019.

Saha, P., Dash, S., and Mukhopadhyay, S. Physics-incorporated convolutional recurrent neural networks for source identification and forecasting of dynamical systems, 2021.

Sauter, S. A. and Schwab, C. Boundary element methods. 2011.

Seo, Y., Defferrard, M., Vandergheynst, P., and Bresson, X. Structured sequence modeling with graph convolutional recurrent networks, 2016.

Shang, C., Chen, J., and Bi, J. Discrete graph structure learning for forecasting multiple time series, 2021.

Shi, X., Chen, Z., Wang, H., Yeung, D.-Y., kin Wong, W., and chun Woo, W. Convolutional lstm network: A machine learning approach for precipitation nowcasting, 2015.

Simonovsky, M. and Komodakis, N. Dynamic edge-conditioned filters in convolutional neural networks on graphs, 2017.

Smith, J. D., Azizzadenesheli, K., and Ross, Z. E. Eikonet: Solving the eikonal equation with deep neural networks, 2020.

Tompson, J., Schlachter, K., Sprechmann, P., and Perlin, K. Accelerating eulerian fluid simulation with convolutional networks, 2017.

Toth, P., Rezende, D. J., Jaegle, A., Racanière, S., Botev, A., and Higgins, I. Hamiltonian generative networks, 2020.

Vaswani, A., Shazeer, N., Parmar, N., Uszkoreit, J., Jones, L., Gomez, A. N., Kaiser, L., and Polosukhin, I. Attention is all you need, 2017.

Veličković, P., Cucurull, G., Casanova, A., Romero, A., Liò, P., and Bengio, Y. Graph attention networks, 2018.

Ying, L., Biros, G., and Zorin, D. A kernel-independent adaptive fast multipole algorithm in two and three dimensions. *Journal of Computational Physics*, 196(2):591–626, 2004. ISSN 0021-9991. doi: <https://doi.org/10.1016/j.jcp.2003.11.021>. URL <https://www.sciencedirect.com/science/article/pii/S0021999103006090>.

Yu, B., Yin, H., and Zhu, Z. Spatio-temporal graph convolutional networks: A deep learning framework for traffic forecasting. *Proceedings of the Twenty-Seventh International Joint Conference on Artificial Intelligence*, Jul 2018. doi: 10.24963/ijcai.2018/505. URL <http://dx.doi.org/10.24963/ijcai.2018/505>.

Zhao, L., Song, Y., Zhang, C., Liu, Y., Wang, P., Lin, T., Deng, M., and Li, H. T-gcn: A temporal graph convolutional network for traffic prediction. *IEEE Transactions on Intelligent Transportation Systems*, 21(9):3848–3858, Sep 2020. ISSN 1558-0016. doi: 10.1109/tits.2019.2935152. URL <http://dx.doi.org/10.1109/TITS.2019.2935152>.

Çağatay Yıldız, Heinonen, M., and Lähdesmäki, H. Ode²vae: Deep generative second order odes with bayesian neural networks, 2019.

A. Notation and Method Supplementary

A.1. Glossary of notations

Symbol	Used for
t	Time or timestamps.
\mathbf{x}	Spatial locations.
\mathbf{x}_{new}	Spatial locations which are unseen by models during training.
u	Physical quantities or continuous signals with spatial location and time as input.
$N(\mathbf{x})$	neighborhood of \mathbf{x} .
F	Mapping of historical observations into future predictions.
a_t	Parametric function in parametric PDEs.
\mathcal{L}_{a_t}	Differential operator in parametric PDEs.
\mathcal{F}	Operator for solving the parametric PDEs, mapping parametric function to solution function.
\mathcal{F}^\dagger	Operator for approximating true operators in the parametric PDEs.
\mathcal{K}_{a_t}	Kernel operator as an instance of \mathcal{F}^\dagger for solving the parametric PDEs.
\mathcal{G}	Operator of groundtruth.
\mathcal{G}^\dagger	Universal Operator to approximate the operator of groundtruth.
c, ξ, θ, η	Parameters in universal operator.
v^{enc}	Solution representation function obtained by encoders.
v^{dec}	Solution representation function obtained by decoders.
P	Projector to map u into v .
P'	Projector to map back v into u .

Table 6. Glossary of Notations used in this paper.

A.2. Multipole graph construction

Neighborhood construction. The neighborhood system is constructed by ϵ -ball, which can be written as for point \mathbf{x} ,

$$\begin{cases} d(\mathbf{x}, \mathbf{x}_i) \leq \epsilon & \mathbf{x}_i \in N(\mathbf{x}); \\ d(\mathbf{x}, \mathbf{x}_i) > \epsilon & \mathbf{x}_i \notin N(\mathbf{x}). \end{cases} \quad (15)$$

$d(\mathbf{x}, \mathbf{y})$ is the distance between point \mathbf{x} and \mathbf{y} . In the planar dataset, the $d(\mathbf{x}, \mathbf{y})$ is calculated by

$$d(\mathbf{x}, \mathbf{y}) = \|\mathbf{x} - \mathbf{y}\|_2, \quad (16)$$

while in the sphere dataset, the distance term is calculated by

$$d(\mathbf{x}, \mathbf{y}) = \arccos(\langle \mathbf{x}, \mathbf{y} \rangle). \quad (17)$$

Multipole graph kernel algorithm. The multipole method is to use a series of sparse and low-rank matrix to approximate the true kernel matrix. The true kernel matrix is decomposed into a hierarchy of low-rank structures. First, all the spatial points are randomly divided into L levels, and for each level $1 \leq l \leq L$, the graph message passing is firstly operated inter-level, as

$$v_t^{\text{enc},(l)}(\mathbf{x}) = (\mathcal{K}_{a_t} v_t^{(l)})(\mathbf{x}), \quad (18)$$

Then, the low-level points' representation will be used to update the high-level one, as

$$v_t^{\text{enc},(l+1)}(\mathbf{x}) = (\mathcal{K}_{a_t} v_t^{(l)})(\mathbf{x}), \quad (19)$$

and the high-level points' representation will be also used to update the points of low level reversely, as

$$v_t^{\text{enc},(l)}(\mathbf{x}) = (\mathcal{K}_{a_t} v_t^{(l+1)})(\mathbf{x}). \quad (20)$$

It can be regarded as decomposing the kernel with a series of low-rank matrix by recursively applying the three steps. And for each point, it can aggregate messages from neighbors of different levels, and thus the recursive structure of the algorithm can allow each point to be affected farther points, although it consumes more time.

B. A ODE-based Decoder

We establish another decoder based on Neural ODE (Chen et al., 2019). The ODE-based decoder is constructed by

$$\frac{\partial u(\mathbf{x}, t)}{\partial t} = (\mathcal{L}_{a_t} u_t)(\mathbf{x}). \quad (21)$$

$$(22)$$

In this way, we first use a universal operator \mathcal{F} to approximate \mathcal{L}_{a_t} , and then use the Neural ODE, reads

$$\begin{aligned} \frac{du(\mathbf{x}, t)}{dt} &= (\mathcal{F} u_t)(\mathbf{x}), \\ u(\mathbf{x}, t) &= \int_0^t (\mathcal{F} u_\tau)(\mathbf{x}) d\tau, \end{aligned} \quad (23)$$

For our model aims to handle the long-term prediction, the ‘backward’ process is extremely slow, thus we regard it as computational infeasible. Table 7 gives the comparison on ODE-based decoder and non-ODE-based decoder on the dataset of Solar Energy and Humidity on one epoch, and the performance comparison. Because the ODE-based decoder is extremely time-consuming, thus we did not conduct experiments on other datasets to show its effectiveness. It shows that our model is superior to the ODE-based one in terms of both computational efficiency and prediction accuracy, because the over-fitting effects are extremely obvious in ODE-based one.

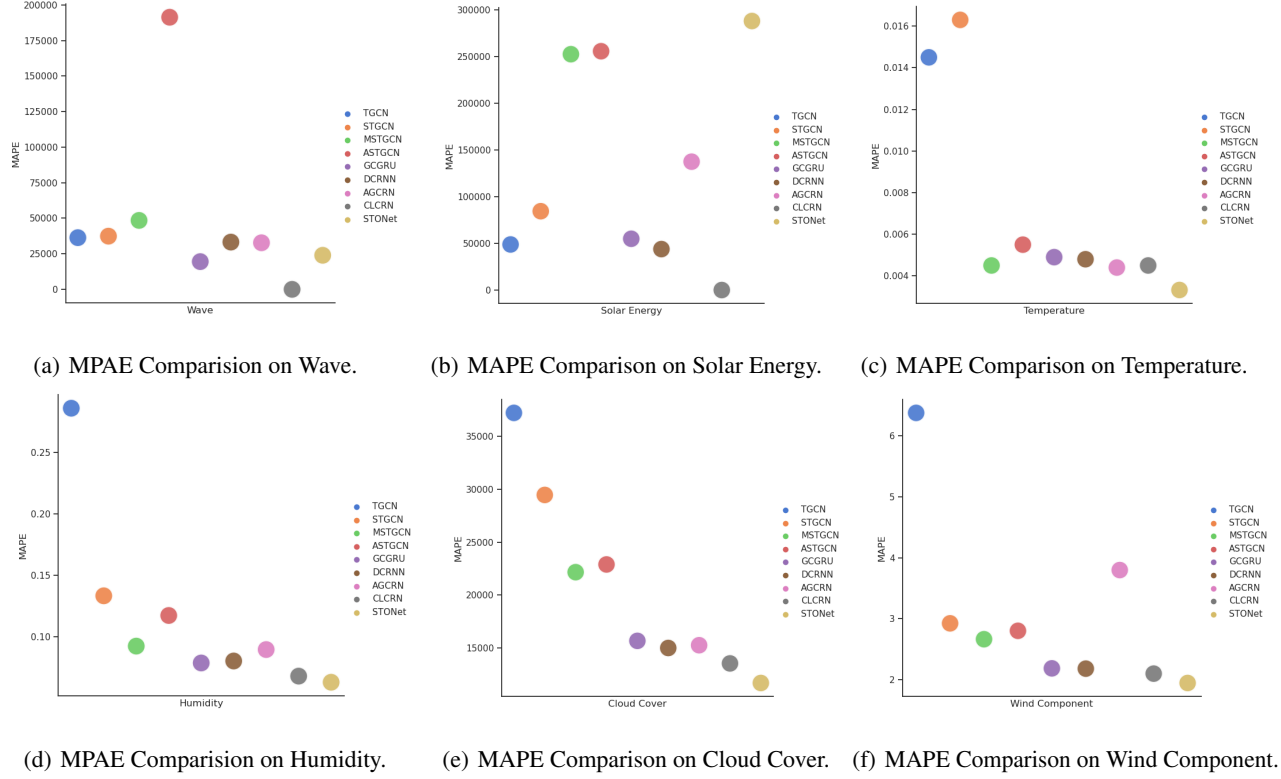


Figure 8. Model Performance Comparison on MAPE.

Table 7. Comparison on different decoder type on Dataset of Humidity and Solar Energy. ‘Time’ is the one epoch training time cost by the method. The test is implemented on a single Nvidia-V100(32510MB).

Datasets		Humidity			
Decoder Type	set	MAE	RMSE	Memory	Time
ODE-based	train	3.1491 \pm 0.4533	7.1483 \pm 0.0991	13641MB	
	test	12.083 \pm 6.2098	17.2462 \pm 9.5624	12'37"	
Non-ODE-based		Solar Energy			
Decoder Type	set	MAE	RMSE	Memory	Time
ODE-based	train	0.6466 \pm 0.0610	0.8975 \pm 0.1312	22957MB	63'07"
	test	2.0103 \pm 0.4933	2.1439 \pm 0.3534	25183MB	
Non-ODE-based	test	0.4273 \pm 0.0256	0.6584 \pm 0.0287	10'42"	

C. Experiment Supplementary

C.1. Method description

(1) TGCN is proposed for traffic forecasting, with the traffic sensors’ graph constructed according to the road distance. The spatial convolution is based on Vanilla GCN, which uses the normed Laplacian matrix as the aggregation operator, and its temporal dynamics is modeled by GRU.

(2) STGCN is also proposed for traffic forecasting. Different from TGCN, its temporal dynamics is modeled

by 1DConv.

(3) MSTGCN which is established for traffic forecasting, its spatial dependency is captured by ChebConv, which is a higher-order version of Vanilla GCN, approximating the graph spectral filters by Chebyshev polynomials.

(4) ASTGCN as a traffic forecasting model, is fully attention based, with spatial dependency captured by graph-attention mechanisms, and temporal dynamics captured by series self-attention.

(5) GCGRU uses high order ChebConv to replace the linear transformation layers in GRU. It is established for many multi-variate time series forecasting tasks.

(6) AGCRN trains the node embeddings, with the product of two node embeddings as their similarity, to adaptively construct the semantic graph as spatial dependency. It is established for many multi-variate time series forecasting tasks, not only limited in traffic forecasting.

(7) CLCRN as a spatio-temporal meteorological forecasting model, employs the conditional local convolution which is established for spherical datasets, and based on the assumption of smoothness of local patterns in weather forecasting. It is the state-of-the-art method for

geophysical quantities forecasting.

C.2. Model comparison

Metrics computation. Let

$$\mathbf{U}^{(t_1, t_{n_t})} = [u(\mathbf{X}, t_1), \dots, u(\mathbf{X}, t_{n_t})] \quad (24)$$

$$\hat{\mathbf{U}}^{(t_1, t_{n_t})} = [\hat{u}(\mathbf{X}, t_1), \dots, \hat{u}(\mathbf{X}, t_{n_t})] \quad (25)$$

be the ground truth and the predictions obtained by neural networks respectively. The three metrics including MAE, RMSE and MAPE are calculated as

$$\text{MAE}(\mathbf{U}^{(t_1, t_{n_t})}, \hat{\mathbf{U}}^{(t_1, t_{n_t})}) = \frac{1}{n_t} \sum_{i=1}^{n_t} |\hat{u}(\mathbf{X}, t_i) - u(\mathbf{X}, t_i)| \quad (26)$$

$$\text{RMSE}(\mathbf{U}^{(t_1, t_{n_t})}, \hat{\mathbf{U}}^{(t_1, t_{n_t})}) = \frac{1}{n_t} \sqrt{\sum_{i=1}^{n_t} |\hat{u}(\mathbf{X}, t_i) - u(\mathbf{X}, t_i)|^2} \quad (27)$$

$$\text{MAPE}(\mathbf{U}^{(t_1, t_{n_t})}, \hat{\mathbf{U}}^{(t_1, t_{n_t})}) = \frac{1}{n_t} \sum_{i=1}^{n_t} \frac{|\hat{u}(\mathbf{X}, t_i) - u(\mathbf{X}, t_i)|}{|u(\mathbf{X}, t_i)|} \quad (28)$$

MAPE comparison. Here we give the metrics of MAPE obtained by different methods, shown in Fig. 8. MAPE metrics is not stable, because there exists a term in the denominator, and thus we do not consider the contributions of terms with ground truth equaling 0. However, for datasets Wave, Solar Energy and Cloud Cover, the minimal is still extremely small, causing the MAPE term extremely large. Therefore, we think the comparison of MAPE on these three datasets are not meaningful.

C.3. Spatially-inductive forecasting

Data preprocess. The nodes in each dataset need to be re-divided into nodes for training and nodes for inductive evaluation. The detailed processing is

- For Wave, The nodes are originally sampled from 64×64 images, so we randomly choose another 512 nodes to evaluate models' spatially-inductive forecasting ability.
- For Solar Energy: Since it is a dataset with low-resolution, we randomly choose 108 nodes for training, and the rest 29 nodes are used for inductive evaluation.
- For the weather datasets: We first downsample the resolution to 16×32 , with 512 nodes used for training, and randomly choose another 512 different nodes for inductive evaluation.

Fig. 13 gives further details on spatially-inductive forecasting on all datasets except Solar Energy, because the

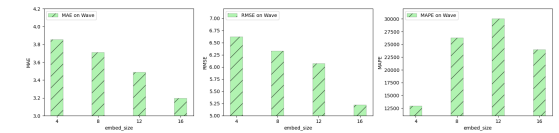
inductive ratio is always fixed for such a dataset of low spatial resolution. It shows that with the increase of the inductive 'Ratio', the prediction accuracy decreases. However, all the deviations are very small and acceptable.

C.4. Temporally-irregular forecasting

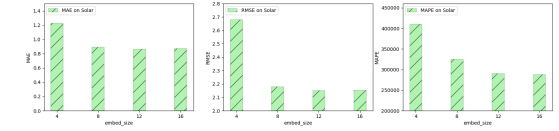
Fig. 14 gives further details on temporally-irregular forecasting on all datasets except Solar Energy. As the output timestamps' labels fed in the model decrease, the predictive performance decrease due to excessive loss of supervised signals and information.

C.5. Ablation Study

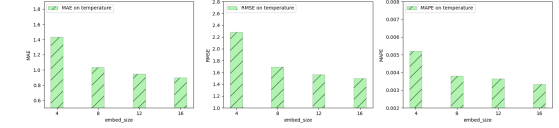
For each dataset, we give ablation study on the four hyper-parameters, which are 'embedding size', 'layer number', 'level numbers' and 'weight of reconstruction loss'. The change of performance with the change of hyper-parameters is shown in Fig. 9, 10, 11 and 12 respectively.



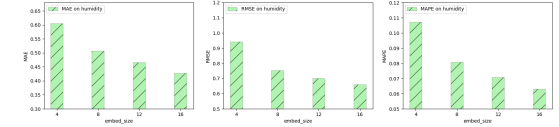
(a) Change of metrics with 'Embedding Size' on Wave.



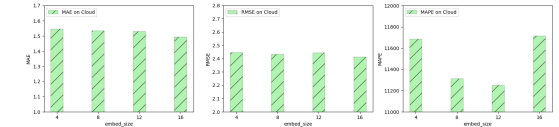
(b) Change of metrics with 'Embedding Size' on Solar Energy.



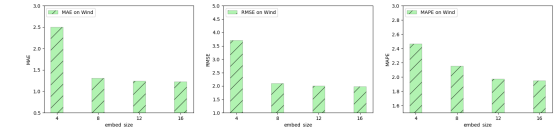
(c) Change of metrics with 'Embedding Size' on Temperature.



(d) Change of metrics with 'Embedding Size' on Humidity.



(e) Change of metrics with 'Embedding Size' on Cloud Cover.



(f) Change of metrics with 'Embedding Size' on Wind Component.

Figure 9. Model Performance Comparison on 'Embedding Size'.

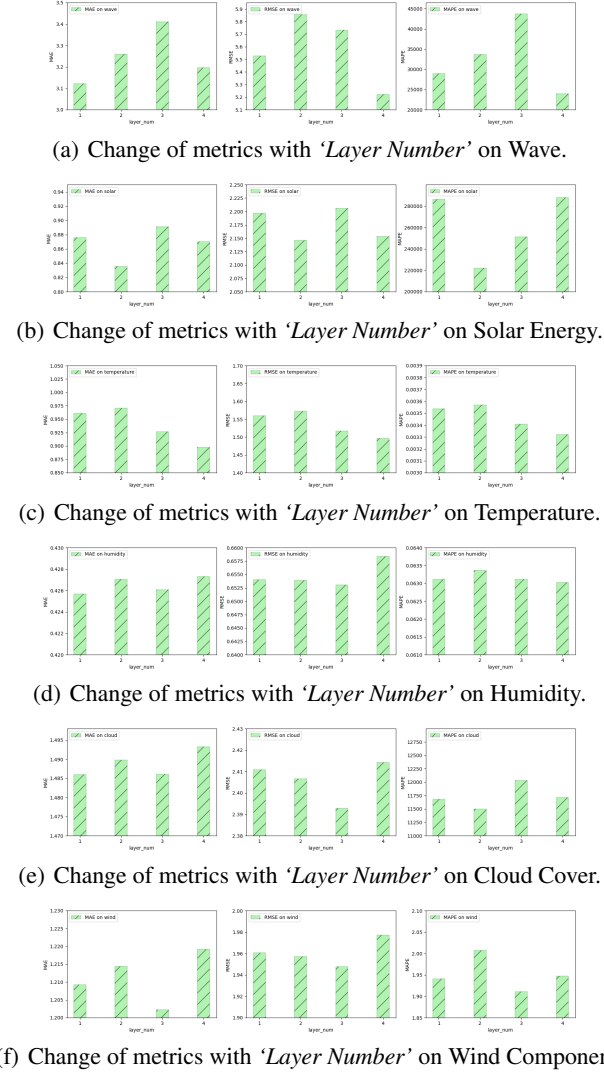


Figure 10. Model Performance Comparison on 'Layer Number'.

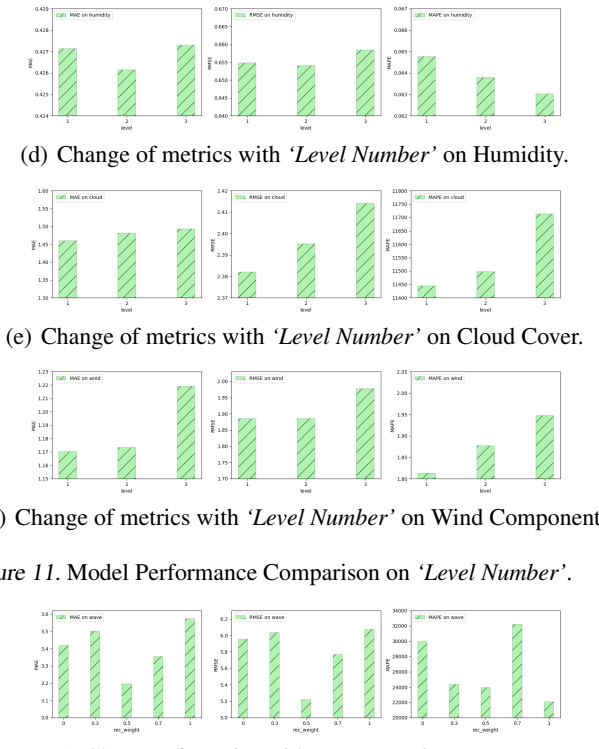


Figure 11. Model Performance Comparison on 'Level Number'.

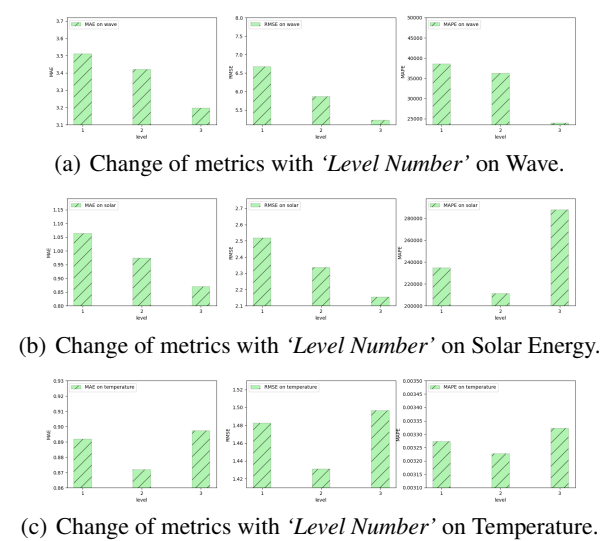
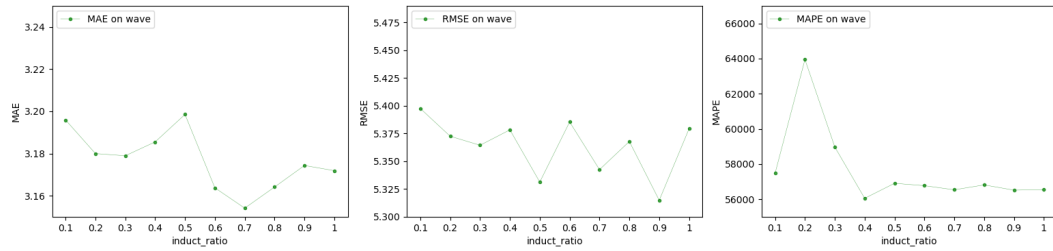
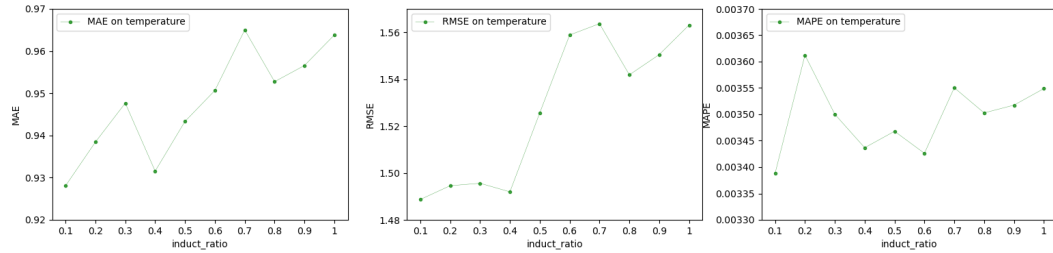


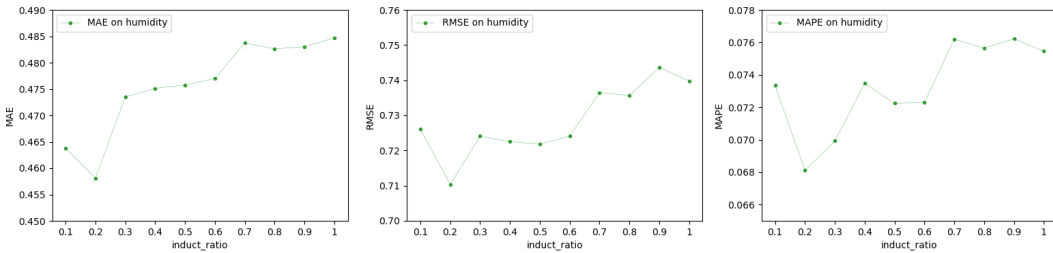
Figure 12. Model Performance Comparison on 'Loss Weight'.



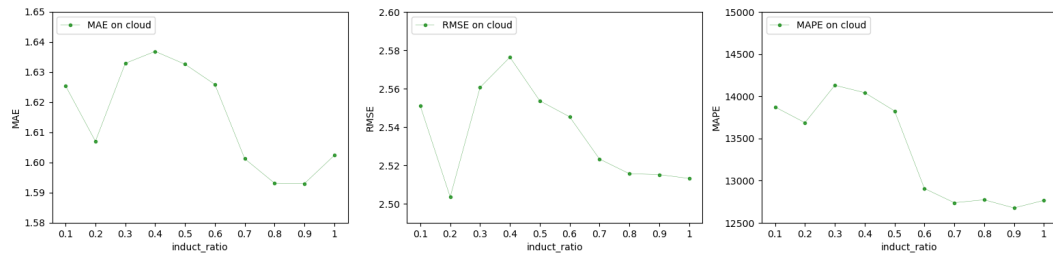
(a) Change of metrics with 'Ratio' on Wave.



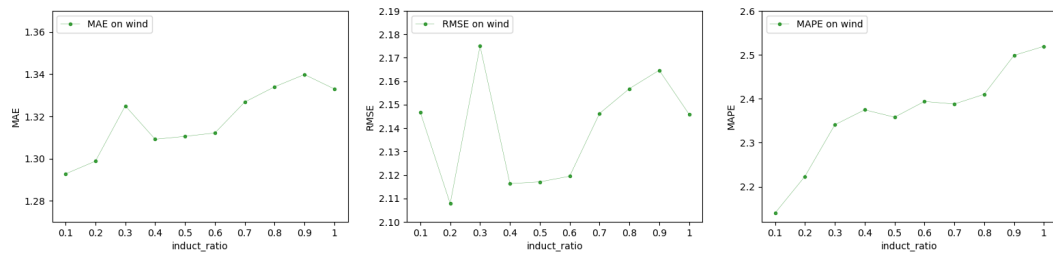
(b) Change of metrics with 'Ratio' on Temperature.



(c) Change of metrics with 'Ratio' on Humidity.



(d) Change of metrics with 'Ratio' on Cloud Cover.



(e) Change of metrics with 'Ratio' on Wind Component.

Figure 13. Model performance with the change of inductive points' 'Ratio'.

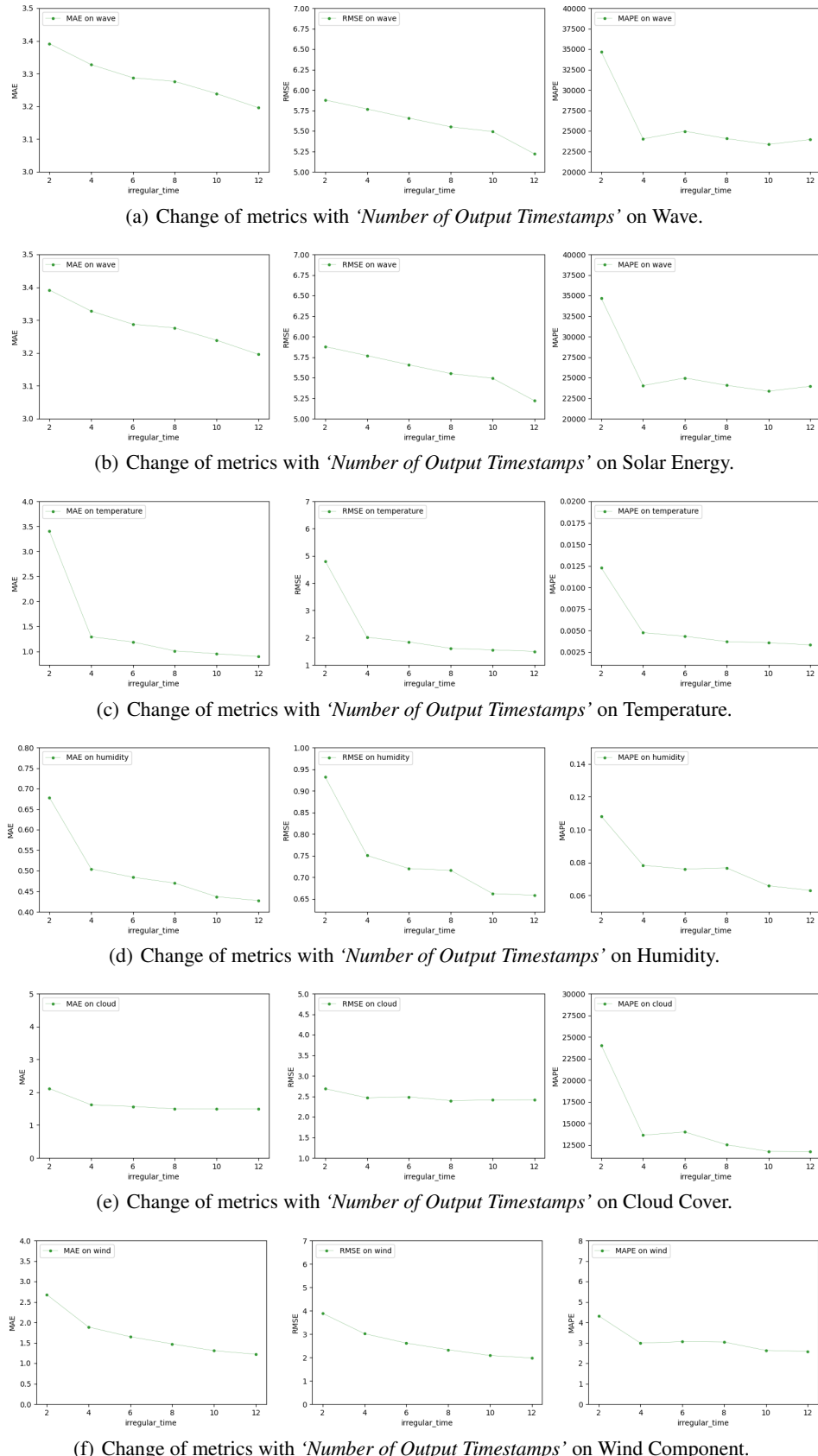


Figure 14. Model performance with the change of 'Number of Output Timestamps'.